Unsupported Pt3Ni Aerogels as Corrosion Resistant PEFC Anode Catalysts under Gross Fuel Starvation Conditions

Author(s):
Henning, Sebastian; Shimizu, Ryo; Herranz, Juan; Kuehn, Laura; Eychmueller, Alexander; Uchida, Makoto; Kakinuma, Katsuyoshi; Schmidt, Thomas

Publication date:
2018-01-06

Permanent link:
https://doi.org/10.3929/ethz-b-000265148

Originally published in:
Journal of the Electrochemical Society 165(6), https://doi.org/10.1149/2.0531802jes

JES Focus Issue on Proton Exchange Membrane Fuel Cell (PEMFC) Durability

Unsupported Pt_3Ni Aerogels as Corrosion Resistant PEFC Anode Catalysts under Gross Fuel Starvation Conditions

Sebastian Henning,[1,=,*] Ryo Shimizu,[2,=] Juan Herranz,[2,,z] Laura Kühn,[3] Alexander Eychmüller,[3] Makoto Uchida,[4,**] Katsuyoshi Kakinuma,[4,**] and Thomas J. Schmidt[1,5,**]**

[1]*Electrochemistry Laboratory, Paul Scherrer Institut, 5232 Villigen, Switzerland*
[2]*Interdisciplinary Graduate School of Medicine and Engineering, University of Yamanashi, Kofu, 400-8511, Japan*
[3]*Physical Chemistry, Technische Universität Dresden, 01062 Dresden, Germany*
[4]*Fuel Cell Nanomaterials Center, University of Yamanashi, Kofu, 400-0021, Japan*
[5]*Laboratory of Physical Chemistry, ETH Zurich, 8093 Zurich, Switzerland*

Mitigating catalyst corrosion is crucial for the commercial success of polymer electrolyte fuel cells (PEFCs). Novel catalysts that can withstand the harsh conditions in case of gross fuel (i.e. H_2) starvation events at the PEFC anode are needed to increase the fuel cell stack's service life and to meet the durability targets set for automotive applications. To make progress in this respect, we have tested an unsupported, bimetallic Pt_3Ni alloy (aerogel) catalyst at the PEFC anode and subjected it to a stress test that mimics the high potentials ($\geq$ 1.5 V vs. the reversible hydrogen electrode) encountered upon fuel starvation. In contrast to commercial carbon-supported platinum catalysts (Pt/C), the Pt_3Ni aerogel displays excellent durability and performance retention in end-of-life fuel cell polarization curves. Additionally, the aerogel catalyst shows ≈35% higher surface-specific activity for the hydrogen oxidation/evolution reaction than Pt/C. These results highlight the great potential of using novel unsupported catalysts at the anode of PEFCs.

 [DOI: 10.1149/2.0531802jes]

Manuscript submitted November 9, 2017; revised manuscript received December 22, 2017. Published January 6, 2018. *This paper is part of the JES Focus Issue on Proton Exchange Membrane Fuel Cell (PEMFC) Durability.*

Polymer electrolyte fuel cells (PEFCs) customarily rely on platinum nanoparticles supported on carbon (Pt/C) to catalyze the anodic hydrogen oxidation and the cathodic oxygen reduction reactions (HOR and ORR, respectively, leading to anode and cathode sometimes being referred to as hydrogen- and oxygen-electrodes).[1,2] Among the latter, the ORR is catalytically more demanding, and thus higher Pt loadings are implemented in PEFC cathodes vs. anodes (up to ≈0.4 vs. ≈0.05 mg_{Pt}/cm^2_{geom}).[3] Irrespectively of this activity difference, both anodic and cathodic Pt/C catalysts suffer from significant corrosion of the carbon support during the high potential excursions (> 1 V vs. the reversible hydrogen electrode, V_{RHE}) concomitant to PEFC operation, which limits the device's service life.[4] Potentials $\geq$ 1.5 V_{RHE} on the cathode side can for instance be caused by PEFC start-up/shut-down and local fuel starvation.[5,6] To minimize the damage of these start-up/shut-down events, technical solutions like a high-flow air purge of the anode compartment that minimizes the residence time of the H_2/air anode front have been developed.[7] On the other hand, complete absence of fuel in the anode compartment under load leads to the so called gross hydrogen starvation. This is typically triggered by the blockage of hydrogen gas inlets in an individual anode flow field by liquid water which, in order to sustain the cell current, leads to an anode potential increase up to a value at which water oxidation and carbon support corrosion can occur.[8] Most importantly, unlike in the start-up/shut-down degradation discussed above, these hydrogen starvation issues are difficult to overcome by engineering solutions.[9] Alternatively, material-based mitigation strategies include composite anode electrodes exhibiting high HOR and oxygen evolution reaction (OER) activity, as well as corrosion-resistant, non-carbon supported or even completely support-free catalysts.[9]

Inspired by the latter approach, and motivated by our recent results with PEFC cathodes from unsupported Pt_3Ni aerogel catalysts that demonstrate excellent stability during start-up/shut-down accelerated stress tests (ASTs),[10,11] this work investigates the applicability of the same material as an anode catalyst. For this purpose, the current-potential (I/E curve) performance of Pt_3Ni aerogel anodes is first compared to that obtained with commercial Pt/C catalysts. Next, the durability of these anode catalysts in an AST that simulates gross hydrogen starvation is investigated. As we will demonstrate below, the Pt_3Ni aerogel has a higher surface-specific HOR activity than Pt/C and, unlike the latter material, shows excellent stability throughout the applied AST, therefore constituting an extremely promising PEFC anode catalyst.

Experimental

Synthesis.—Pt_3Ni aerogel was synthesized according to the procedure described in reference 12. In brief, 0.585 ml of a 0.205 M H_2PtCl_6 solution (8 wt. % in H_2O, Sigma Aldrich) and 4 ml of a freshly prepared 10 mM $NiCl_2$ solution ($NiCl_2$*$6H_2O$, 99%, Sigma Aldrich) were diluted in 790 ml of ultrapure water (18.2 MΩ cm, Millipore) and stirred until the mixing was complete. Next, 7.0 ml of freshly prepared 0.1 M $NaBH_4$ solution (granular, 99.99%, Sigma Aldrich) were added while stirring vigorously. A brown solution was obtained that was kept stirring for another 30 min. Subsequently, the reaction solution was distributed among several 100 ml vials. After about four days, black Pt_3Ni hydrogel formed at the bottom of the containers. The hydrogel was washed with water and the solvent was exchanged with acetone afterwards. These anhydrous gels were subjected to critical point drying in CO_2 (Critical Point Dryer 13200J–AB, SPI Supplies), which resulted in the final aerogel material.

Electron microscopy analysis.—For tomography and cross section preparation, a Zeiss NVision 40 focused ion beam scanning electron microscope (FIB-SEM) with a Ga^+ beam source was employed. Samples were prepared by fixing catalyst coated membranes on SEM holders using carbon tape and conductive silver glue, followed by carbon sputtering (tens of nm) to further increase conductivity.

Membrane electrode assembly preparation.—Membrane electrode assemblies (MEAs) were fabricated using Pt_3Ni aerogel, Pt on high surface area carbon (Pt/CB, 47 wt% Pt, TKK, TEC10E50E)

=These authors contributed equally to this work.
*Electrochemical Society Student Member.
**Electrochemical Society Member.
zE-mail: juan.herranz@psi.ch

or Pt on graphitized carbon black (Pt/GCB, 30 wt% Pt, TKK, TEC10EA30E) as the anode catalyst (with loadings of 0.05 ± 0.01 mg_{Pt}/cm^2_{geom}), Nafion XL–100 (DuPont) as the membrane and commercial gas diffusion electrodes (Johnson Matthey, 0.4 mg_{Pt}/cm^2_{geom} HISPEC 9100 Pt/HAS on Sigracet GDL 25 BC) as the cathode. Catalyst inks for Pt_3Ni electrodes were prepared as described in reference 10 by mixing 5 mg of catalyst, 0.7 mg of K_2CO_3 (99.995% trace metals basis, Sigma Aldrich), 18 mg of Na^+–exchanged Nafion solution (prepared from a 1:2 volumetric mixture of 0.1 M NaOH and Nafion solution,[13] and equal to a Nafion–to–catalyst-ratio of 0.12) and 1.0 ml of an 8 wt% aqueous isopropanol solution (ultrapure water, 18.2 MΩ cm, Elga Purelab Ultra and isopropanol, 99.9%, Chromasolv Plus for HPLC, Sigma Aldrich). After ultrasonication (USC100T, 45 kHz, VWR) for 30 minutes and spray coating (using a frame to confine the coating to an active area of 1 cm^2), the resulting catalyst coated membranes (CCMs) were immersed into 1 M H_2SO_4 solution (96%, Suprapur, Merck) overnight (≈16 hours), followed by rinsing with ultrapure water and drying under ambient conditions. The acid washing step was introduced to remove the filler material K_2CO_3 and thus to create a catalyst layer with increased porosity (for details see reference 10). For Pt/CB (Pt/GCB) anodes, 50 mg of catalyst was mixed with 500 (650) mg of 5 wt% Nafion solution (equal to a Nafion–to–carbon-ratio of 1.0) and 4.5 ml of a 20 wt% aqueous isopropanol solution, followed by the steps described above without the acid washing. In a last step, the CCMs were hotpressed at 120°C and 1 bar/cm^2_{geom} for 5 minutes to a gas diffusion layer (GDL 25 BC, Sigracet) and a commercial gas diffusion electrode (see above) on the anode and cathode sides, respectively. For the preparation of low Pt-loaded electrodes (with ≈5 $\mu g_{Pt}/cm^2_{geom}$), 5 mg of Pt_3Ni (Pt/CB, Pt/GCB) was mixed with 90 (45, 30) mg of Ketjenblack (EC-600JD, AkzoNobel), 1800 (950, 650) mg of 5 wt% Nafion solution (equal to a Nafion–to–carbon-ratio of 1.0) and 8.5 (4.5) ml of a 20 wt% aqueous isopropanol solution, followed by the steps described above.

PEFC tests.—The MEAs were placed in a differential fuel cell that allows studies under homogeneous, well-defined conditions in the absence of along–the–channel effects such as changing temperature, relative humidity (RH) and gas concentration.[14] The fuel cell used for this study was developed inhouse, featuring 5 parallel channels of 1 mm width over an active area of 1 cm^2.[15] Using steel spacers with defined thickness, cell compression was set such that ≈25% compression of the gas diffusion media was obtained.[15,16] The MEA break-in started by drawing the maximum current that would yield cell potentials > 0.6 V in H_2/O_2 at 1.5 bar_{abs} and a relative humidity (RH) of 100% at 25 and 80°C (1 hour each, flow rates anode/cathode: 300/750 ml/min,[17] stoichiometries ≥ 30/≥ 30), followed by cooling down of the cell, activating potential cycles and a repetition of the first step (at 80°C). It must be noted here that even as the applied stoichiometry ratios are significantly higher than for technical cells, the gas flow velocities remain in the same order of magnitude due to the reduced size of the device.[14]

Cyclic voltammograms (CVs) of the PEFC anode catalyst were measured after break-in at 25°C and 100% RH, scanning the working electrode's (i.e. PEFC anode's) potential between 0.075 and 1.0 V_{RHE} at 50 mV/s, with a H_2 flow rate of 50 ml/min at the counter/reference electrode (i.e. PEFC cathode side) and the working electrode N_2 flow halted just prior to the measurement. The corresponding electrochemical surface area (ECSA) value was averaged from the H–adsorption and H–desorption charges between 0.09 and 0.4 V_{RHE} after double-layer correction, assuming a conversion factor of 210 $\mu C/cm^2_{Pt}$.[18] To perform CO stripping experiments,[19] the working electrode potential was held at 0.1 V_{RHE} for 35 min, while the counter/reference electrode was purged with 50 ml/min of 5% H_2 in N_2. For the first 10 min, the working electrode was purged with 5% CO in N_2 at 50 ml/min, followed by 25 min purging with pure N_2 at 300 ml/min to remove the non-adsorbed CO. CO oxidation currents were obtained by subtracting a subsequent CV from the CO stripping CV (at 50 mV/s), and the resulting oxidation charges were converted into ECSAs assuming a conversion factor of 420 $\mu C/cm^2_{Pt}$.[20] H_2-crossover tests were conducted by recording a linear potential sweep from 0.6 to 0.1 V_{RHE} with a scan rate of 1 mV/s at 80°C, 100% RH, 1.5 bar_{abs}, an anode H_2 flow rate of 300 ml/min and a cathode N_2 flow rate of 750 ml/min, respectively;[21] the H_2–crossover current densities typically amounted to ≈2 mA/cm^2_{MEA}.

All I/E curves were recorded at 80°C and 100% RH with anode/cathode flow rates of 300/750 ml/min (stoichiometries ≥ 30/≥ 30) at 1.5 bar_{abs} for either H_2/O_2 or H_2/air, using a Biologic VSP-300 potentiostat with a 10A/5V current booster. The measurement was done galvanostatically, whereby the cell current was stabilized for 3 minutes at each data point and the data was averaged from the last 2 minutes. Concomitantly, the cell resistance (R_Ω) was determined for each data point by galvanostatic electrochemical impedance spectroscopy (1 MHz to 1 Hz). Mass- and surface-specific activites for H_2/O_2 operation were extracted at 0.9 V_{RHE} after correcting potential and current for cell resistance and H_2–crossover, respectively.

The accelerated stress tests used to mimic PEFC anode degradation upon H_2 starvation (whereby the anode potential transitions from an HOR-operative value of ≈0 V_{RHE} to ≥ 1.5 V_{RHE})[8,9,22–25] were performed at 80°C, 100% RH, ambient pressure, cathode H_2 flow of 100 ml/min and anode N_2 flow of 100 ml/min. More specifically, the inhouse-developed AST protocol consisted of 250 potential cycles in a square wave voltammetry pattern between 0 and 1.5 V_{RHE} with a holding time of 10 s at upper and lower potential limit, respectively.

H_2-pump tests.—To determine the H_2-oxidation/evolution reactivity and mass transport properties of the PEFC anode catalyst layers, H_2-pump experiments were performed by connecting the anode outlet (i.e. H_2-pump working electrode) to the cathode inlet and setting the H_2 flow rate to 300 ml/min; measurements were performed at ≈120% RH and with p_{H2} ≈ 1.0 bar. Hydrogen oxidation and evolution (HER) polarization curves were recorded at 2 mV/s at 80°C; galvanostatic electrochemical impedance spectroscopy (1 MHz to 1 Hz) to determine R_Ω was performed at 0.1, 0.25 and 0.5 A/cm^2_{geom}, respectively. To determine the proton resistance along the working electrode (i.e. PEFC anode) catalyst layer ($R_{H+,anode}$), potentiometric electrochemical impedance spectroscopy tests were conducted at 0.2 V_{RHE} (with a 1 mV perturbation) while operating at 80°C and with fully humidified N_2 and H_2 feeds at the anode (working) and cathode (counter), respectively.[26,27]

Results and Discussion

First, the performance of Pt_3Ni aerogel anodes using an application-relevant loading of ≈0.05 mg_{Pt}/cm^2_{geom} was tested in the PEFC, whereby commercial GDEs with 0.4 mg_{Pt}/cm^2_{geom} served as the respective cathodes (see Experimental section for details). The aerogel's anode performance was compared to the one displayed by anodes prepared from commercial Pt nanoparticle catalyst materials, supported on high surface area carbon (Pt/CB) or a more corrosion resistant graphitized carbon black (Pt/GCB),[28] again using anode vs. cathode loadings of ≈0.05 vs 0.4 mg_{Pt}/cm^2_{geom}. The beginning-of-life (BOL) I/E curves in H_2/O_2 and H_2/air condition in Figures 1A/1B are identical for Pt_3Ni aerogel and commercial Pt/CB and Pt/GCB anodes, demonstrating the aerogel's applicability as an anode catalyst. Additionally, similar mass-specific ORR activities at 0.9 V_{RHE} of ≈140 ± 10 A/g_{Pt} were determined for all MEAs (not shown), whereby the latter is a typical value for the Pt/C catalyst used on the cathode when tested under equivalent conditions.[18]

Motivated by the promising initial performance of Pt_3Ni anodes, this MEA and the ones from carbon-supported catalysts were subjected to an inhouse-developed accelerated stress test that simulates gross fuel starvation events, in which the anode potential increases from the ≈0 V_{RHE} at which the HOR typically takes place to ≥ 1.5 V_{RHE}.[8,9,22–25] To be precise, the AST consisted of 250 square wave voltammogram (SWV) cycles on the anode between 0 and 1.5 V_{RHE} with holding times of 10 s at each potential, as illustrated by the inset in Figure 1B. As discernable from the end-of-life (EOL) I/E curves, significant performance deterioration is observed for the

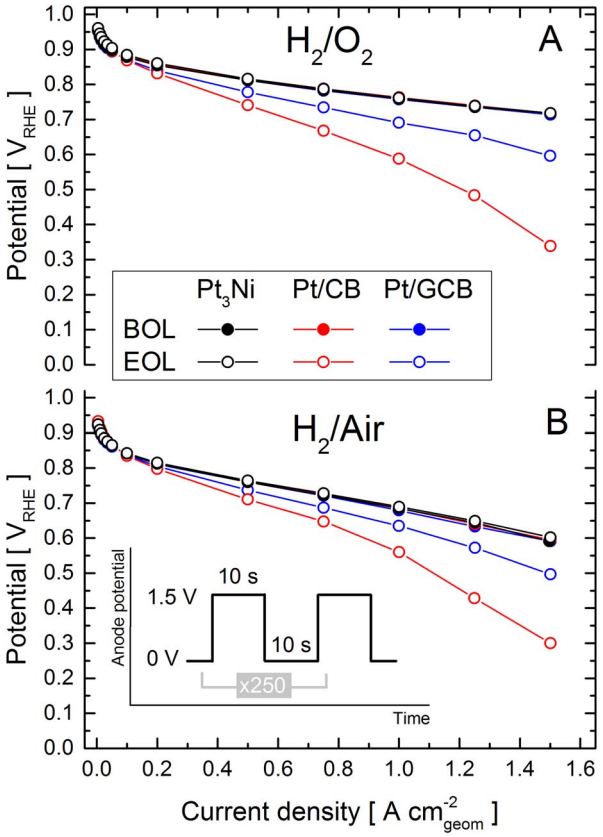

Figure 1. Beginning- and end-of-life (BOL, EOL) I/E curves at 80°C, 100% RH in (A) H_2/O_2 and (B) H_2/air at 1.5 bar_{abs} for Pt_3Ni aerogel, Pt/CB and Pt/GCB MEAs (with loadings of 0.05 ± 0.01 mg_{Pt}/cm^2_{geom} for all anodes). The inset in B illustrates the performed accelerated stress test protocol in which the anode potential is stepped 250 times between 0 and 1.5 V_{RHE} with holds of 10 s at each potential. Note the overlap among BOL I/E curves for all three catalysts, as well as with the EOL curve for Pt_3Ni aerogel.

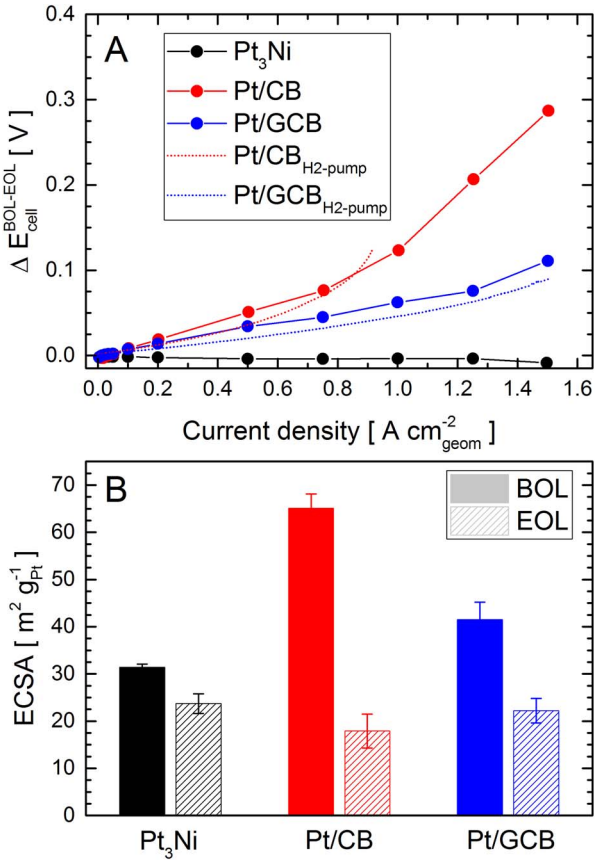

Figure 2. (A) Potential difference between BOL/EOL I/E curves (cf. Figure 1 – solid lines and symbols) and H_2-pump polarization curves (cf. Figure 3 – dotted lines), corresponding to the change of the anodic overpotential during the AST for Pt_3Ni aerogel, Pt/CB and Pt/GCB MEAs with anode loadings of 0.05 ± 0.01 mg_{Pt}/cm^2_{geom}. (B) BOL and EOL ECSA values at 25°C, averaged on the basis of two independent experiments.

MEAs with commercial Pt/CB and Pt/GCB anodes (whereby the overpotential at 1.5 A/cm^2_{geom} increased by ≈300 and ≈100 mV, respectively), whereas no losses occur for the MEA implementing the Pt_3Ni aerogel as the anode catalyst.

To assign the causes for these performance losses, we consider the different overpotential contributions to the overall cell potential (E_{cell}) formulated in Equation 1:[18,21]

$$E_{cell} = E_{rev} - iR_{\Omega} - \eta_{HOR} - iR_{H+,\,anode} - \eta_{tx,\,anode} - \eta_{ORR} - iR_{H+,cathode} - \eta_{tx,\,cathode} \quad [1]$$

where E_{rev} is the thermodynamic, reversible potential, i is the current density, R_{Ω} is the cell (i.e. high frequency) resistance, η_{HOR} and η_{ORR} are the HOR and ORR kinetic overpotentials, and R_{H+} and η_{tx} refer to the proton transfer resistance and mass transport overpotential along the anode and cathode catalyst layers, respectively. Since during the degradation protocol the cathode remained at a harmless potential of ≈0 V_{RHE} that should not affect the catalyst layer's kinetic, proton transfer and mass transport properties, the corresponding overpotential terms are expected to remain unmodified in the course of the H_2 starvation AST (i.e. $\eta_{ORR}{}^{BOL} \approx \eta_{ORR}{}^{EOL}$, $R_{H+,cathode}{}^{BOL} \approx R_{H+,cathode}{}^{EOL}$ and $\eta_{tx,cathode}{}^{BOL} \approx \eta_{tx,cathode}{}^{EOL}$). This hypothesis is further supported by the constant I/E curve performance of Pt_3Ni MEAs along the AST, and thus the BOL vs. EOL potential differences for Pt/CB and Pt/GCB are tentatively ascribed to changes on the anode side. Additionally, BOL and EOL impedance measurements (cf. Figure SI-1) point at a negligible increase of the cell resistance in the AST ($R_{\Omega}{}^{BOL} \approx R_{\Omega}{}^{EOL}$), and the absence of a characteristic 45° line allowing for the quantification of $R_{H+,anode}$ can be attributed to negligible proton transfer resistance along the anode catalyst layers (i.e. $R_{H+,anode}{}^{BOL} \approx R_{H+,anode}{}^{EOL} \approx 0$).[26,27] Therefore, the difference between beginning- and end-of-life cell performance ($\Delta E_{cell}{}^{BOL-EOL}$) can be exclusively assigned to changes in the HOR kinetics and anode mass transport overpotentials, according to Equation 2:

$$\Delta E_{cell}^{BOL-EOL} = \eta_{HOR}^{EOL} - \eta_{HOR}^{BOL} + \eta_{tx,anode}^{EOL} - \eta_{tx,anode}^{BOL} \quad [2]$$

Thus, Figure 2A displays this difference between BOL and EOL potentials derived from the subtraction of the R_{Ω}-corrected I/E curves in Figure 1. Additionally, AST-induced changes in all three catalysts' ECSAs are summarized in Figure 2B, whereby the ≈25% loss of surface area displayed by the Pt_3Ni aerogel is in stark contrast with the ECSA decays of ≈75% and ≈50% undergone by Pt/CB and Pt/GCB, respectively. Considering the upper potential of 1.5 V_{RHE} applied in the AST, this decrease of Pt dispersion is not only ascribable to a growth of the Pt nanoparticles (caused by migration and/or Ostwald ripening) that could lead to a change of their HOR catalytic properties (assuming an ECSA effect on the η_{HOR} terms in Eq. 2 – see discussion below), but also to nanoparticle detachment due to the corrosion of the carbon support, which could modify the catalyst layer's mass transport properties (i.e. $\eta_{tx,anode}$ in Eq. 2), as it has been established for PEFC cathodes.[29–32]

In an attempt to further differentiate these kinetic and mass transport contributions to the overall performance loss (cf. η_{HOR} and $\eta_{tx,anode}$ in Equation 2), the recording of polarization curves at the beginning and end of the AST was followed by H_2-pump experiments (see Experimental section for details), whereby the combination of the high Pt loading of the commercial cathode GDE (0.4 mg_{Pt}/cm^2_{geom})

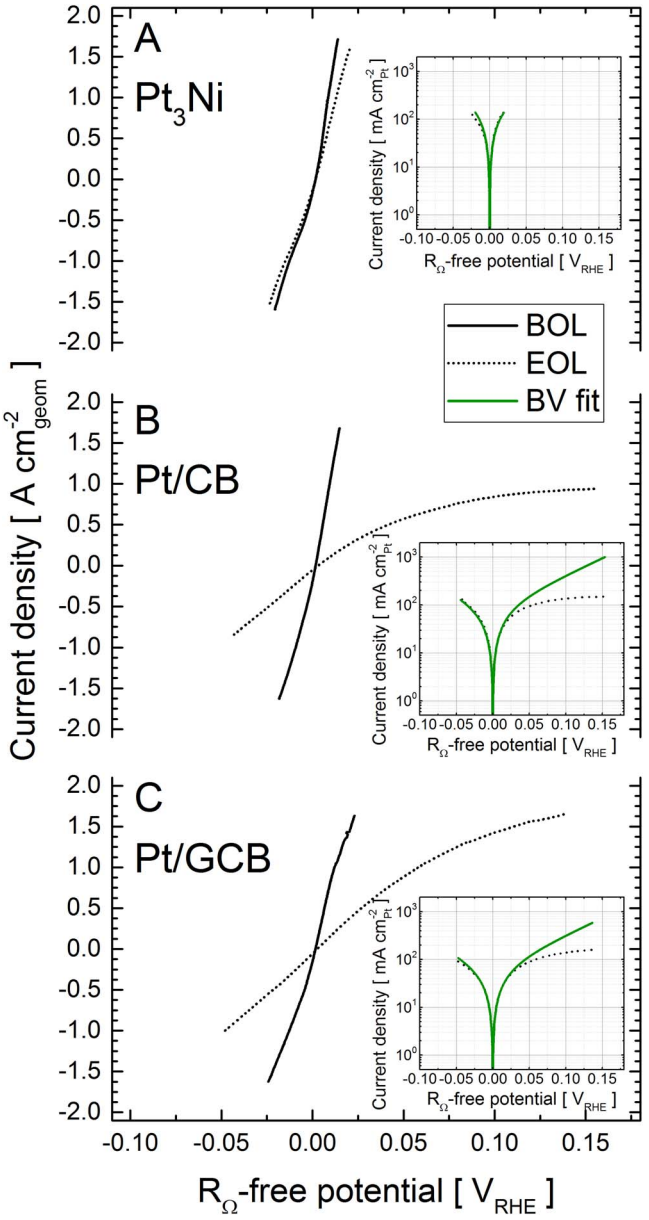

Figure 3. Hydrogen oxidation and evolution polarization curves (80°C, ≈120% RH, p_{H2} ≈ 1.0 bar, 2 mV/s) at beginning- and end-of-life (BOL, EOL) in terms of geometric current densities vs. R_Ω-corrected potential in an H_2-pump configuration for (A) Pt_3Ni, (B) Pt/CB and (C) Pt/GCB catalyst layers with loadings of 0.05 ± 0.01 mg_{Pt}/cm^2_{geom}. The insets show EOL, ECSA-normalized H_2-oxidation/evolution current densities and their corresponding fit to the Butler-Volmer equation (green). Note that the latter fits have been computationally extended beyond the corresponding fitting ranges (± 1.0 and ± 0.5 A/cm^2_{geom} for Pt_3Ni and Pt/CB / Pt/GCB, respectively), as to illustrate the difference between kinetically controlled and measured (i.e. projected vs. transport limited) currents in the HOR-branch.

and the extremely fast HER/HOR kinetics on Pt[3,33,34] ensure that reference/counter electrode-side (i.e. PEFC cathode) contributions to the measured I/E response remain minor (i.e. the measured electrochemical performance is exclusively representative of the Pt_3Ni, Pt/CB or Pt/GCB catalyst layers in the anode side of the original fuel cell).

With these considerations, Figure 3 displays the hydrogen oxidation/evolution polarization curves recorded in these H_2-pump experiments, whereby the measured potential was corrected for the cell resistance $R_{\Omega,}$ obtained from the high frequency real axis intercept of impedance spectra recorded at 0.1, 0.25 and 0.5 A/cm^2_{geom}, which typically amounted to ≈45 $m\Omega\ cm^2_{geom}$. An additional correction for the proton transport losses in the anode catalyst layer (CL) was omitted due to the negligible contribution compared to R_Ω (cf. above and references 3, 34). Consistent with the excellent durability displayed in the H_2/O_2 and H_2/air PEFC tests before and after the AST measurements (Figure 1), the H_2-pump polarization curves in Figure 3A recorded on the Pt_3Ni aerogel at beginning- and end-of-life almost completely overlay, indicating minimal kinetic and/or mass transport losses. On the other hand, the overall potential increase induced by the AST and inferred from the comparison of BOL and EOL hydrogen oxidation/evolution polarization curves for Pt/CB and Pt/GCB (see Figures 3B and 3C) qualitatively confirms that the performance degradation in the subtracted PEFC polarization curves (Fig. 2A) is the result of severe losses in anode kinetic and mass transport properties. In this respect, the same subtractive approach discussed above for the PEFC polarization curves can be extended to the H_2-pump BOL and EOL data, yielding the AST-induced HOR-losses represented as a dotted line in Figure 2A − whereby the good agreement among performance losses in I/E curve and H_2-pump experiments (cf. solid vs. dotted lines in Figure 2A) again supports that the degradation occurs exclusively on the anode side. Moreover, while the BOL H_2-pump curves follow an exponential proportionality between current and overpotential expected for a kinetically-controlled process (i.e. $\log(i) \propto \eta$), indicative of an absence of mass transport limitations over the complete range of investigated current densities, the EOL polarization curves of Pt/CB and Pt/GCB deviate from the purely kinetic response derived from the fitting to the Butler-Volmer equation (see the discussion below) at current densities above ≈0.5 A/cm^2_{geom} (cf. Figures 3B and 3C plus insets), pointing at significant mass transport limitations by the end of the AST.

To understand the reason for the profound increase in $\eta_{tx,anode}$ of Pt/CB anodes, their catalyst layer structure was investigated by scanning electron microscopy and compared to the one of Pt_3Ni anodes. The BOL top-view and cross-sectional images in Figure SI-2A and SI-2B show that the Pt_3Ni aerogel catalyst does not cover the entire membrane surface and is instead distributed in the form of chunks with diameters <5 μm. Pt/CB CLs (cf. Figure SI-2D and SI-2E) on the other hand cover the membrane completely, whereas the catalyst thickness varies significantly. The average thickness was estimated to be ≈30 $\mu m/(mg_C\ cm^{-2}_{geom})$ which is in excellent agreement with the value reported in literature of ≈28 ± 2 $\mu m/(mg_C\ cm^{-2}_{geom})$.[35] After the AST, however, the Pt/CB CL in Figure SI-2F displays a thickness reduction of ≈50%, down to ≈15 $\mu m/(mg_C\ cm^{-2}_{geom})$, which can explain the increase in $\eta_{tx,anode}$. At the same time, no changes of the CL morphology were observed for Pt_3Ni anodes (cf. Figure SI-2C), which is consistent with the purely kinetically-controlled performance in H_2-pump experiments discussed above. In contrast to Pt/CB, the structural integrity of Pt/GCB CLs appears to be less affected by the AST, specifically with respect to the catalyst layer's thickness, since no significant thinning is observed in the cross-sectional SEM images in Figure SI-2H/I. These observations from the cross section image analysis further agree with the evolution of ECSAs throughout the AST in Figure 2B discussed above, whereby the ECSA loss of ≈75% experienced by Pt/CB reflects the drastic changes in its CL structure. Moreover, the behavior of Pt_3Ni and Pt/CB under high potential excursions is comparable to our own findings in previous works,[10,11] whereby the Pt/CB degradation in separated potential regimes of 0.6–1.0 and 1.0–1.5 V_{RHE} (somehow decoupling the effects observed in the 0–1.5 V_{RHE} tests included herein) was related to Pt-nanoparticle growth and carbon support corrosion, respectively.[7,8,31,32,36] As in the EOL I/E curves in Figure 1, the deterioration of Pt/GCB (ECSA loss ≈50%) is worse than that of Pt_3Ni aerogel, but less severe than for Pt/CB, highlighting the advantage of working with more corrosion-stable carbon supports.[7]

Next, we quantified the changes in the anodes' HOR kinetic losses in the course of the AST by extracting the hydrogen oxidation overpotential (η_{HOR}) from Figures 3A–3C; the latter overpotential was estimated at a surface-specific current density of 50 mA/cm^2_{Pt}, which

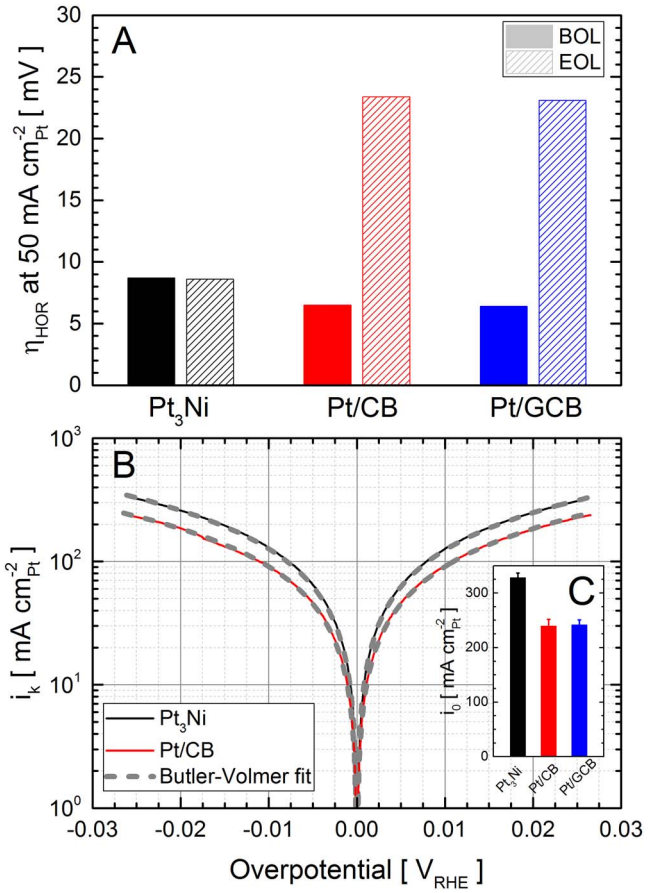

Figure 4. (A) Hydrogen oxidation overpotentials (η_{HOR}) at 50 mA/cm$^2_{Pt}$ in H_2-pump experiments (cf. Figure 3) prior to and after the AST (BOL, EOL) for Pt_3Ni, Pt/CB and Pt/GCB MEAs (with anode loadings of ≈50 $\mu g_{Pt}/cm^2_{geom}$), respectively. (B) ECSA-normalized H_2-oxidation/evolution kinetic current densities (positive going scans, 80°C, ≈120% RH, p_{H2} ≈1.0 bar, 2 mV/s) for carbon-diluted Pt_3Ni and Pt/CB MEAs (anode loading ≈5 $\mu g_{Pt}/cm^2_{geom}$), and their corresponding fit to the Butler-Volmer equation (dashed lines). (C) Exchange currents density (i_0) values estimated from the fits in panel B for carbon-diluted Pt_3Ni, Pt/CB and Pt/GCB MEAs (anode loading ≈5 $\mu g_{Pt}/cm^2_{geom}$), respectively.

corresponds to an area-specific current density < 0.5 A/cm$^2_{geom}$, i.e. below the clear onset of mass transport limitation observed for Pt/CB and Pt/GCB (cf. insets in Figures 3B and 3C). The comparison of the BOL and EOL η_{HOR}-values in Figure 4A indicates a constant overpotential of ≈8 mV for Pt_3Ni aerogel, whereas Pt/CB and Pt/GCB show an increase from ≈6 to ≈23 mV throughout the AST. This increase is a somehow puzzling result since, as it will be discussed below, the decrease of ECSA caused by the AST (cf. Figure 2B) is not expected to lead to changes in the surface-specific HER/HOR activity. Additionally, the H_2-oxidation/evolution exchange current densities (i_0) at BOL and EOL were tentatively extracted from the hydrogen oxidation and evolution polarization curves. Based on previous studies in which anodic and cathodic transfer coefficients for the HER/HOR on Pt were shown to add up to one, a simple Butler-Volmer equation was used for fitting the polarization curves:[33,37]

$$i_k = i_0\, L\, A \left[e^{\frac{\beta F}{RT}\eta} - e^{-\frac{(1-\beta)F}{RT}\eta} \right] \qquad [3]$$

where i_k is the kinetic current density (assumed to be equal to the measured current density within the designated fitting range), L is the anode Pt loading (g_{Pt}/cm^2_{geom}), A is the ECSA (m^2_{Pt}/g_{Pt}, cf. Figure 2B), β is the symmetry factor, F is the Faraday constant (96485 C/mol), R is the universal gas constant (8.3145 J/(K mol)) and T is the temperature (353 K).

The i_0-values derived from these fittings are summarized in Figure SI-3 and amount to ≈150 vs. ≈200 mA/cm$^2_{Pt}$ for Pt_3Ni aerogel vs. Pt/CB and Pt/GCB at BOL, respectively. Interestingly, these values are lower than the ones reported in the literature for Pt/C catalysts (≈250 mA/cm$^2_{Pt}$)[34,37] – a difference that we attribute to the application-relevant, high electrode loadings of ≈50 $\mu g_{Pt}/cm^2_{geom}$ used in the fuel cell starvation experiments in this work, which are ≈25-fold larger than the ≈2 $\mu g_{Pt}/cm^2_{geom}$ implemented for the study of HOR-kinetics in references 33, 34, 37. Specifically, the combination of these high anode loadings with the ultra-fast kinetics of H_2-oxidation/evolution on Pt leads to extremely large currents even at very low potentials, which makes the derivation of i_0 values extremely sensitive to small errors, e.g. in the determination of R_Ω. Additionally, the ratio of cathode/anode Pt loading only amounts to a factor of ≈8, and thus the overall I/E response can be affected by the limited speed of the reaction on the counter/reference electrode (i.e. former PEFC cathode) side. Consequently, the values plotted in Figure SI-3 for high electrode loadings of ≈50 $\mu g_{Pt}/cm^2_{geom}$ should be regarded as apparent i_0's rather than being fully representative of the catalysts' kinetic behavior.

To mitigate the limitations mentioned above, anodes with lower loadings of ≈5 $\mu g_{Pt}/cm^2_{geom}$ were prepared by diluting Pt_3Ni aerogel, Pt/CB and Pt/GCB with high surface area carbon (see Experimental section for details). This dilution was necessary to reach total (i.e. catalyst plus carbon) electrode loadings of ≈0.05 $mg_{catalyst+C}/cm^2_{geom}$, which constitutes the lower limit for CCM fabrication by our manual spray coating process. Due to the poorly distinguishable H-adsorption/H-desorption currents for these electrodes (caused by the capacitive contribution of the diluting carbon), the ECSAs required for activity surface-normalization were determined by the CO-stripping method (see Figure SI-4 for the corresponding CVs).[20,38] Most importantly, the polarization curves and Butler Volmer-fits are displayed in Figure 4B (for greater clarity only Pt_3Ni and Pt/CB are shown; see Figure SI-5 for Pt/GCB), and the corresponding i_0-values derived from the fits are included in Figure 4C. Besides for the great agreement between measured polarization curves and subsequent fits for both electrodes, the β-value of ≈0.5 and i_0 of ≈240 mA/cm$^2_{Pt}$ derived for Pt/CB and Pt/GCB are similar to the values reported in previous literature,[33,34,37] therefore validating our experimental and fitting approach. More interestingly, however, the higher HER/HOR activity of the Pt_3Ni aerogel (i_0 ≈ 330 mA/cm$^2_{Pt}$) is a further advantage of aerogel anodes, in addition to the enhanced durability discussed above. Even if the exact reason for this activity difference remains elusive for the moment, a similar effect has been reported in a recent study on the HER/HOR activity of $Pt_{0.68}Co_{0.3}Mn_{0.02}$ nanostructured thin film catalysts (for which i_0 ≈ 500 mA/cm$^2_{Pt}$).[39] Moreover, in a combined experimental and theoretical work, Greeley et al. related the HER activities of Pd monolayers on different metals to the free energy of hydrogen adsorption and corresponding variations of the d-band center energy.[40] Considering the well-known effect of alloy formation on the position of the d-band center,[41] the cause for the activity increase observed for the Pt_3Ni aerogel might be the successful formation of an alloy phase in this material, which we confirmed through X-ray absorption spectroscopy measurements discussed in a previous study.[12] On the other hand, the differences in the ECSAs among these materials (i.e. ≈65 m$^2/g_{Pt}$ for Pt/CB, ≈ 42 m$^2/g_{Pt}$ for Pt/GCB and ≈30 m$^2/g_{Pt}$ for Pt_3Ni) can be excluded as a cause for this activity enhancement, since Pt/CB and Pt/GCB show similar i_0's despite their different ECSAs, therefore confirming the absence of a particle size effect for the HER/HOR kinetics on Pt already discussed in several previous studies.[37,42,43]

Coming back to the results of the AST with anode loadings of ≈50 $\mu g_{Pt}/cm^2_{geom}$, the EOL apparent i_0-values of ≈80 mA/cm$^2_{Pt}$ for Pt/CB and Pt/GCB (see Figure SI-3) are significantly lower than the respective BOL values, in agreement with the puzzling increase in η_{HOR} of Figure 4A discussed above. This could indicate that the EOL kinetic values are also affected by imprecisions in the determination of i_0 at high anode loadings (cf. discussion above), and/or that mass transport limitations affect the assessment of these kinetic parameters

even at low current densities ≤ 0.5 A/cm$^2_{geom}$ (see Figure 3). Assuming an ECSA-independent and constant i_0-value of $\approx$240 mA/cm$^2_{Pt}$ and applying Equation 2, the reduction of the ECSA in the AST is expected to result in η_{HOR} increases of mere $\approx$14 and $\approx$8 mV at 1.5 A/cm$^2_{geom}$ for Pt/CB and Pt/GCB, respectively. Comparing these values with the $\approx$300 and $\approx$100 mV increases in the overall anodic overpotential plotted in Figure 2A, it becomes obvious that the deterioration of the catalyst layer structure and concomitant increase of $\eta_{tx,anode}$ during the fuel starvation AST is the dominant reason for the PEFC performance loss observed for the carbon-supported catalyst layers.

Conclusions

In summary, we have demonstrated that unsupported Pt_3Ni aerogel can be employed as an effective PEFC anode catalyst (at loadings of $\approx$0.05 mg$_{Pt}$/cm$^2_{geom}$), showing performance on par with commercial Pt/C materials. Most importantly, the Pt_3Ni aerogel did not display any significant performance losses under gross fuel starvation conditions as simulated by 250 SWV cycles between 0 and 1.5 V_{RHE}. In contrast to this exciting result, Pt/CB and even Pt/GCB showed significant overpotential increases of $>$ 100 mV at 1.5 A/cm$^2_{geom}$ in H_2/O_2 (and H_2/air) I/E curves which were ascribed to anode performance losses after performing H_2-pump experiments on the same electrodes. Specifically, the increase in anodic mass transport overpotential induced by the collapse of the catalyst layer's carbon structure during the AST was identified as the major reason for the performance loss, whereas changes in HOR overpotential were found to have a negligible effect on the AST-induced deterioration of the PEFC performance. Lastly, the higher HER/HOR activity of Pt_3Ni aerogel vs. Pt/C (whereby $i_0 = 330$ vs. 240 mA/cm$^2_{Pt}$, respectively) inferred from H_2-pump experiments with C-diluted electrodes is tentatively assigned to an alloy-induced shift of the aerogel's d-band center, and may constitute an additional advantage of using this unsupported catalyst.

Acknowledgments

This work was funded by the Swiss National Science Foundation (20001E_151122/1), the German Research Foundation (EY 16/18-1) and the European Research Council (ERC AdG 2013 AEROCAT).

ORCID

Juan Herranz https://orcid.org/0000-0002-5805-6192
Thomas J. Schmidt https://orcid.org/0000-0002-1636-367X

References

1. F. T. Wagner, B. Lakshmanan, and M. F. Mathias, *J. Phys. Chem. Lett.*, **1**, 2204 (2010).
2. O. Gröger, H. A. Gasteiger, and J. P. Suchsland, *J. Electrochem. Soc.*, **162**, A2605 (2015).
3. K. C. Neyerlin, W. Gu, J. Jorne, and H. A. Gasteiger, *J. Electrochem. Soc.*, **154**, B631 (2007).
4. A. Rabis, P. Rodriguez, and T. J. Schmidt, *ACS Catal*, **2**, 864 (2012).
5. C. A. Reiser, L. Bregoli, T. W. Patterson, J. S. Yi, J. D. Yang, M. L. Perry, and T. D. Jarvi, *Electrochem. Solid State Lett.*, **8**, A273 (2005).
6. N. Yousfi-Steiner, P. Moçotéguy, D. Candusso, and D. Hissel, *J. Pow. Sourc.*, **194**, 130 (2009).
7. T. Mittermeier, A. Weiß, F. Hasché, G. Hübner, and H. A. Gasteiger, *J. Electrochem. Soc.*, **164**, F127 (2017).
8. T. R. Ralph, S. Hudson, and D. P. Wilkinson, *ECS Trans*, **1**, 67 (2006).
9. P. Rodriguez and T. J. Schmidt, in *Encyclopedia of Applied Electrochemistry*, G. Kreysa, K.-I. Ota, and R. F. Savinell Editors, p. 1606, Springer New York, New York, NY (2014).
10. S. Henning, H. Ishikawa, L. Kühn, J. Herranz, E. Muller, A. Eychmüller, and T. J. Schmidt, *Angew. Chem. Int. Ed.*, **56**, 10707 (2017).
11. S. Henning, J. Herranz, H. Ishikawa, B. J. Kim, D. Abbott, L. Kühn, A. Eychmüller, and T. J. Schmidt, *J. Electrochem. Soc.*, **164**, F1136 (2017).
12. S. Henning, L. Kühn, J. Herranz, J. Durst, T. Binninger, M. Nachtegaal, M. Werheid, W. Liu, M. Adam, S. Kaskel, A. Eychmüller, and T. J. Schmidt, *J. Electrochem. Soc.*, **163**, F998 (2016).
13. J. Suntivich, H. A. Gasteiger, N. Yabuuchi, and Y. Shao-Horn, *J. Electrochem. Soc.*, **157**, B1263 (2010).
14. P. Oberholzer and P. Boillat, *J. Electrochem. Soc.*, **161**, F139 (2014).
15. P. Oberholzer, P. Boillat, A. Kaestner, E. H. Lehmann, G. G. Scherer, T. J. Schmidt, and A. Wokaun, *J. Electrochem. Soc.*, **160**, F659 (2013).
16. P. Oberholzer, P. Boillat, R. Siegrist, A. Kästner, E. H. Lehmann, G. G. Scherer, and A. Wokaun, *Electrochem. Comm.*, **20**, 67 (2012).
17. J. Biesdorf, A. Forner-Cuenca, T. J. Schmidt, and P. Boillat, *J. Electrochem. Soc.*, **162**, F1243 (2015).
18. H. A. Gasteiger, S. S. Kocha, B. Sompalli, and F. T. Wagner, *Appl. Catal. B: Environ.*, **56**, 9 (2005).
19. A. Patrň, A. Rabis, S. E. Temmel, R. Kotz, and T. J. Schmidt, *Catal. Today*, **262**, 161 (2016).
20. F. Maillard, M. Eikerling, O. V. Cherstiouk, S. Schreier, E. Savinova, and U. Stimming, *Faraday Discuss*, **125**, 357 (2004).
21. S. S. Kocha, in *Handbook of Fuel Cells*, W. Vielstich, A. Lamm, and H. A. Gasteiger Editors, John Wiley & Sons, Ltd., Chichester (2010).
22. Y. Shao, G. Yin, and Y. Gao, *J. Pow. Sourc.*, **171**, 558 (2007).
23. S. D. Knights, K. M. Colbow, J. St-Pierre, and D. P. Wilkinson, *J. Pow. Sourc.*, **127**, 127 (2004).
24. Z. Liu, L. Yang, Z. Mao, W. Zhuge, Y. Zhang, and L. Wang, *J. Pow. Sourc.*, **157**, 166 (2006).
25. J. Jung, B. Park, and J. Kim, *Nano. Res. Lett.*, **7**, 34 (2012).
26. Y. Liu, M. W. Murphy, D. R. Baker, W. Gu, C. Ji, J. Jorne, and H. A. Gasteiger, *J. Electrochem. Soc.*, **156**, B970 (2009).
27. Y. Liu, C. Ji, W. Gu, J. Jorne, and H. A. Gasteiger, *J. Electrochem. Soc.*, **158**, B614 (2011).
28. L. Castanheira, W. O. Silva, F. H. B. Lima, A. Crisci, L. Dubau, and F. Maillard, *ACS Catal*, **5**, 2184 (2015).
29. Y. Shao-Horn, W. C. Sheng, S. Chen, P. J. Ferreira, E. F. Holby, and D. Morgan, *Topics Catal*, **46**, 285 (2007).
30. J. Durst, A. Lamibrac, F. Charlot, J. Dillet, L. F. Castanheira, G. Maranzana, L. Dubau, F. Maillard, M. Chatenet, and O. Lottin, *Appl. Catal., B*, **138**, 416 (2013).
31. J. Speder, A. Zana, I. Spanos, J. J. K. Kirkensgaard, K. Mortensen, M. Hanzlik, and M. Arenz, *J. Pow. Sourc.*, **261**, 14 (2014).
32. C. Hartnig and T. J. Schmidt, *J. Pow. Sourc.*, **196**, 5564 (2011).
33. J. Durst, A. Siebel, C. Simon, F. Hasche, J. Herranz, and H. A. Gasteiger, *Energ. Environ. Sci.*, **7**, 2255 (2014).
34. J. Durst, C. Simon, F. Hasche, and H. A. Gasteiger, *J. Electrochem. Soc.*, **162**, F190 (2014).
35. W. Gu, D. R. Baker, Y. Liu, and H. A. Gasteiger, in *Handbook of Fuel Cells*, W. Vielstich, A. Lamm, and H. A. Gasteiger Editors, John Wiley & Sons, Ltd., Chichester (2010).
36. S. J. Ashton and M. Arenz, *J. Pow. Sourc.*, **217**, 392 (2012).
37. J. Durst, C. Simon, A. Siebel, P. J. Rheinländer, T. Schuler, M. Hanzlik, J. Herranz, F. Hasché, and H. A. Gasteiger, *ECS Trans*, **64**, 1069 (2014).
38. K. J. J. Mayrhofer, D. Strmcnik, B. B. Blizanac, V. Stamenkovic, M. Arenz, and N. M. Markovic, *Electrochim. Acta*, **53**, 3181 (2008).
39. X. Wang, R. K. Ahluwalia, and A. J. Steinbach, *J. Electrochem. Soc.*, **160**, F251 (2013).
40. J. Greeley, J. K. Nørskov, L. A. Kibler, A. M. El-Aziz, and D. M. Kolb, *ChemPhysChem*, **7**, 1032 (2006).
41. V. Stamenkovic, B. S. Mun, K. J. Mayrhofer, P. N. Ross, N. M. Markovic, J. Rossmeisl, J. Greeley, and J. K. Norskov, *Angew. Chem. Int. Ed.*, **45**, 2897 (2006).
42. H. Uchida, K. Izumi, K. Aoki, and M. Watanabe, *Phys. Chem. Chem. Phys.*, **11**, 1771 (2009).
43. J. Herranz, J. Durst, E. Fabbri, A. Patru, X. Cheng, A. Permyakova, and T. Schmidt, *Nano Energy*, **29**, 4 (2016).